Pergamon

Int. J. Multiphase Flow Vol. 21, No. 4, pp. 639–648, 1995
Elsevier Science Ltd. Printed in Great Britain

0301-9322(95)00007-0

A LAGRANGIAN–EULERIAN SCHEME FOR FLOW AROUND AN AIRFOIL IN RAIN

J. R. VALENTINE and R. A. DECKER
University of Utah, Salt Lake City, UT 84112, U.S.A.

(Received 26 September 1993; in revised form 23 January 1995)

Abstract—In the interest of assessing airfoil performance in rain, a Lagrangian particle tracking algorithm for a general body-fitted co-ordinate system has been developed and linked with a thin layer incompressible Navier–Stokes code. Non-deforming spherical particles are tracked through the two-dimensional, incompressible air flow field surrounding a NACA 64-210 airfoil section. Each tracked particle represents a distribution of raindrops. Impacts on the airfoil surface and the resulting splashback are modeled, and the steady state fluid field and droplet distribution are determined utilizing an iterative, two-way momentum coupled approach. Details of the splashback effect on the boundary layer are examined. A 1–2° rain-induced decrease in stall angle of attack is predicted.

Key Words: two-phase flow, particle tracking, body-fitted grid, Lagrangian simulation, airfoil in rain

1. INTRODUCTION

Several major microburst-related aviation accidents have occurred during extremely heavy rainfall in recent years and have sparked an interest in heavy rain effects on airfoil and aircraft performance in rain. Experimental data indicate that an airfoil in heavy rain is subject to an overall degradation of performance (Bezos & Campbell 1993; Bezos *et al.* 1992; Bilanin 1987; Dunham 1987). In cases where the airfoil boundary layer is predominantly laminar, the performance loss has been mimicked by tripping the boundary layer on the dry airfoil to turbulence (Dunham 1987; Hansman & Craig 1987). For the more general case where the airfoil boundary layer is predominantly turbulent, the performance loss appears to be the result of a rain-induced premature boundary layer separation (Dunham 1987). Two major mechanisms have been hypothesized as contributing to the performance loss: (1) an uneven water film effectively roughens the airfoil surface and (2) splashed back droplets from raindrop impacts are accelerated by air flow field, de-energizing the boundary layer and leaving it more susceptible to separation. The current project attempts to model the latter mechanism through a Lagrangian particle tracking scheme for a general body-fitted co-ordinate system. External viscous flow fields around airfoils are generally determined with a body-fitted grid. In this case, the same grid is used to track particles, allowing for the easy determination of particle field statistics throughout the grid.

Two approaches have been used to model fluid–particle flows. These models have been reviewed by Decker & Schafer (1989) and Durst *et al.* (1984), among others. The Eulerian approach treats both the dispersed particulate and continuous fluid phases as continua and solves Eulerian conservation equations for each. Interphase exchanges of mass, momentum and energy are included as source terms in the appropriate conservation equations. This model is most easily implemented when particles are of a uniform size.

The Lagrangian approach solves Eulerian conservation equations for the continuous fluid phase then integrates Lagrangian equations of motion for the dispersed phase, tracking individual particles through the flow field. A one-way coupled model assumes that the particle motion is influenced by the continuous fluid phase, but the fluid phase is unaffected by the presence of the particles. A two-way coupled model accounts for the two-way exchange of momentum (and mass and energy if applicable) between the dispersed and continuous phases. Source/sink terms are included in the fluid conservation equations and contributions from the particle field are determined. Two approaches have been used in Lagrangian two-way coupled models: a non-iterative transient scheme where the evolution of the particle and fluid flow fields are considered

simultaneously (Dukowisc 1980), and the iterative particle source in cell (PSI-Cell) method (Crowe *et al.* 1977) where the fluid and particle fields are considered separately and updated iteratively until a stationary solution is reached.

In this study, the steady state fluid field and particle distribution are determined around a NACA 64-210 airfoil through a two-way momentum coupled Lagrangian approach. The incompressible, two-dimensional air flow field is determined with a flux-difference splitting code for the thin layer approximation of the Navier–Stokes equations. Lagrangian equations of motion are used to track non-evaporating (thus there is no mass coupling between the phases) and non-deforming spherical particles through the air flow field. An analysis by Bilanin (1987) has indicated that the evaporation of droplets near the airfoil surface should not degrade the lift characteristics of an airfoil. The particulate phase is assumed to be dilute enough that particle collisions can be neglected. Raindrop impacts on the airfoil surface and the resulting splashback of droplets into the flow field are modeled.

2. NUMERICAL METHOD

2.1. Fluid Phase

The air flow field is determined with FMC1, a three-dimensional flux-difference splitting code for the thin-layer approximation of the incompressible Navier–Stokes equations (Hartwick & Hsu 1988; Hartwich & Hall 1990). The code has been modified to account for momentum coupling between the phases as discussed later in the section on interphase coupling.

The computational domain consists of an O–H grid around a NACA 64-210 airfoil section, a spanwise cross section of which is shown in figure 1. Grid dimensions are $m = 45$ normal to the surface (ξ), by 3 spanwise (η), by $n = 143$ circumferential (ζ). There is no variation of the flow field in the spanwise direction. The air flow field is been determined for an airfoil of chord length 1 m and a Reynolds number of $\mathrm{Re} = 2.6 \times 10^6$. The eddy viscosity turbulence model in FMC1 is activated 5% of the chord length from the leading edge of the airfoil; in wind tunnel simulations of airfoils in rain, the boundary layer is generally tripped at about this point.

Airfoil performance is measured in terms of lift and drag coefficients. Lift coefficient is defined as

$$c_l = \frac{F_l}{\frac{1}{2}\rho V_\infty^2 c} \qquad [1]$$

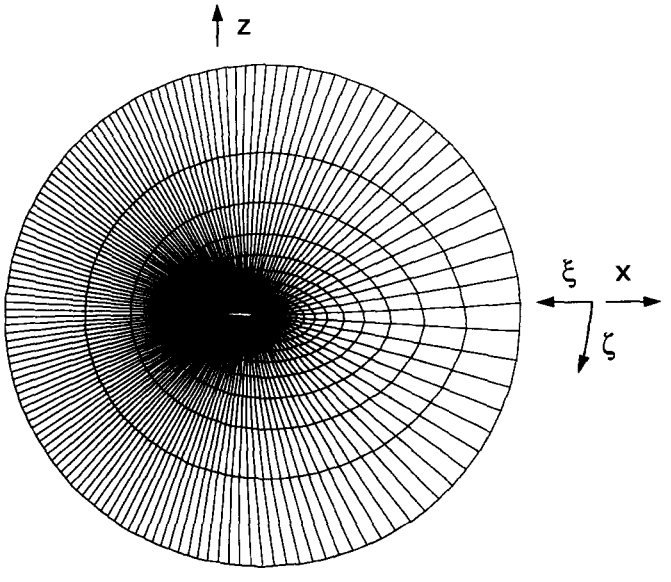

Figure 1. Spanwise cross-section of computational grid surrounding the airfoil. y and η are spanwise.

and drag coefficient as

$$c_d = \frac{F_d}{\frac{1}{2}\rho V_\infty^2 c}, \qquad [2]$$

where F_l and F_d are the sum of the viscous and pressure forces acting on the airfoil in the streamwise and stream normal directions, respectively.

2.2. *Particulate Phase*

2.2.1. *Tracking algorithm*

Particles are assumed to be non-deforming spheres subject only to gravity and drag forces. For small particles with densities much greater than that of the surrounding air, the dimensionless equation of motion for a particle can be written

$$\frac{d\mathbf{V}_p}{dt} = \frac{3\rho c C_D |\mathbf{V} - \mathbf{V}_p|}{8 r_p \rho_p}(\mathbf{V} - \mathbf{V}_p) + \frac{c}{V_\infty^2}\mathbf{g} \qquad [3]$$

where $\mathbf{V}$ and $\mathbf{V}_p$ are the air and particle velocity vectors, $\mathbf{g}$ is the acceleration due to gravity, ρ and ρ_p are the air and particle material densities and r_p is the particle radius. Velocities in [3] are scaled by the free stream air velocity V_∞, lengths by the airfoil chord length c and time by c/V_∞. For a spherical particle, the particle drag coefficient C_D in [3] can be represented over a wide range of particle Reynolds numbers by (Wallis 1969).

$$C_D = \max\left\{0.44, \frac{24}{\mathrm{Re}_p}(1 + 0.15\,\mathrm{Re}_p^{0.687})\right\} \qquad [4]$$

where the particle Reynolds number is defined as

$$\mathrm{Re}_p = \frac{\rho |V_\infty(\mathbf{V} - \mathbf{V}_p)| 2 r_p}{\mu}. \qquad [5]$$

The first term inside the braces in [4] applies for particle Reynolds numbers greater than 10^3 while the second is for particle Reynolds numbers up to 10^3.

A second particle trajectory equation is a chain rule expression for the contravariant particle velocity

$$\frac{d\xi_p}{dt} = \xi_x u_p + \xi_y v_p + \xi_z w_p, \qquad [6]$$

where $\xi_p = (\xi_p, \eta_p, \zeta_p)$ is the particle position in the curvilinear body-fitted co-ordinate system, u_p, v_p and w_p are the cartesian components of the particle velocity and subscripts x, y and z indicate partial differentiation with respect to the subscripted variable. The metric vectors in [6] are defined as

$$\boldsymbol{\xi}_x = (\xi_x, \eta_x, \zeta_x), \quad \boldsymbol{\xi}_y = (\xi_y, \eta_y, \zeta_y) \quad \text{and} \quad \boldsymbol{\xi}_z = (\xi_z, \eta_z, \zeta_z) \qquad [7]$$

and are evaluated at the particle position through linear interpolation of the values at adjacent gridpoints. At each gridpoint, the metrics are evaluated by the expressions (Anderson *et al.* 1984)

$$\begin{aligned}
\xi_x &= \frac{(y_\eta z_\zeta - y_\zeta z_\eta)}{J} & \xi_y &= -\frac{(x_\eta z_\zeta - x_\zeta z_\eta)}{J} & \xi_z &= \frac{(x_\eta y_\zeta - x_\zeta y_\eta)}{J} \\
\eta_x &= -\frac{(y_\xi z_\zeta - y_\zeta z_\xi)}{J} & \eta_y &= \frac{(x_\xi z_\zeta - x_\zeta z_\xi)}{J} & \eta_z &= \frac{(x_\xi y_\zeta - x_\zeta y_\xi)}{J} \\
\zeta_x &= \frac{(y_\xi z_\eta - y_\eta z_\xi)}{J} & \zeta_y &= -\frac{(x_\xi z_\eta - x_\eta z_\xi)}{J} & \zeta_z &= \frac{(x_\xi y_\eta - x_\eta y_\xi)}{J}
\end{aligned} \qquad [8]$$

and the determinant of the inverse of the Jacobian of the transformation by

$$J = x_\xi(y_\eta z_\zeta - y_\zeta z_\eta) - x_\eta(y_\xi z_\zeta - y_\zeta z_\xi) + x_\zeta(y_\xi z_\eta - y_\eta z_\xi). \qquad [9]$$

Again the subscripts ξ, η and ζ indicate partial differentiation and the partial derivatives $x_\xi, x_\eta, x_\zeta, y_\xi$, etc. are approximated numerically with second-order accurate finite differences.

Following the example of Crowe *et al.* (1977), [3] is integrated analytically. Over a small time step of particle travel, the fluid velocity and the particle Reynolds number are assumed approximately constant, then integration of [3] yields

$$\mathbf{V}_p^{n+1} = \mathbf{V}^n - (\mathbf{V}^n - \mathbf{V}_p^n)\exp(-D^n \Delta t) + \boldsymbol{g}\frac{c(1-\exp(-D^n\Delta t))}{V_\infty^2 D^n}, \quad [10]$$

where superscripts refer to time level and

$$D^n = \frac{3\rho c C_D |\mathbf{V}^n - \mathbf{V}_p^n|}{8 r_p \rho_p}. \quad [11]$$

The particle position is advanced by integrating [6] numerically with a trapezoidal scheme. The particle position at the end of the current time step is predicted with an explicit Euler scheme, then the contravariant velocity at this position is averaged with the contravariant velocity at the beginning of the time step to advance the position, i.e.

$$\xi_p^{n+1} = \xi_p^n + \frac{1}{2}\left[\left.\frac{d\xi_p}{dt}\right|^n + \left.\frac{d\xi_p}{dt}\right|^*\right]\Delta t, \quad [12]$$

where the superscript * indicates the contravariant particle velocity at the predicted position. At each position a time step is calculated based on a particle residence time of four steps in the current cell.

2.2.2. Rain model

The drop size distribution of thunderstorm rain can be approximated by the expression

$$N(D_p) = N_0 \exp(-\Lambda D_p) \quad [13]$$

where $N(D_p)$ is the number density of rain drops of diameter D_p (in mm) per cubic meter of air, $N_0 = 1.4 \times 10^3$ m^3 mm, $\Lambda = 3.0 \times R^{-0.21}$ and R is the rainfall rate in mm/h (Joss & Waldvogel 1969). For modeling purposes, this continuous distribution is divided into four discrete intervals, each of length $\Delta D_{p,i}$. The number density of raindrops in each diameter interval is given by

$$N(\Delta D_{p,i}) = \int_{\Delta D_{p,i}} N_0 \exp(-\Lambda D_p)\, dD_p, \quad [14]$$

and the average diameter of raindrops in the interval by

$$D_{p,i} = \frac{\int_{\Delta D_{p,i}} D_p N_0 \exp(-\Lambda D_p)\, dD_p}{N(\Delta D_{p,i})}. \quad [15]$$

Particles enter the computational domain from discrete locations around the boundary with an initial horizontal velocity of V_∞ and an initial vertical velocity determined by equating the gravity and vertical drag forces. Each entry location j has an associated area A_j, so the raindrop number flow rate from location j for diameter interval $\Delta D_{p,i}$ can be expressed as

$$\dot{N}_{ij} = N(\Delta D_{p,i})(\mathbf{V}_{p\infty,i} \cdot \mathbf{A}_j) \quad [16]$$

where $N(\Delta D_{p,i})$ is the rain drop number density for diameter interval i from [14] and $(\mathbf{V}_{p\infty,i} \cdot \mathbf{A}_j)$ is the dot product of the freestream velocity of particles of average diameter $D_{p,i}$ and the normal vector to area A_j. Thus for each drop size interval i and each entry location j, one particle is tracked through the domain and has associated with it a raindrop number flow rate $\dot{N}_{ij}$. The average interval diameter $D_{p,i}$ is used as the tracked particle diameter.

In experimental simulations, rain intensity is generally measured in terms of the liquid water content (LWC) of the air or the mass of water per unit volume of air. Assuming thunderstorm rain, the expression relating rainfall rate (R, in mm/h) to LWC (in g/m^3) is easily determined to be (Dunham 1987)

$$\text{LNC} = 0.054\, R^{0.04}. \quad [17]$$

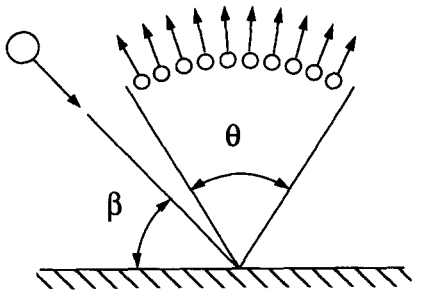

Figure 2. Splashback model showing angle of incidence β and the angular range of splashback θ.

2.2.3. *Splashback model*

Little literature exists on the nature of high speed waterdrop impacts such as those that occur on an airfoil surface in rain. Thus the impact model used here is somewhat arbitrary; however, it is loosely based on experimental observations (Feo 1987) and analytical estimates (Bilanin 1987).

The model used for splashback is shown schematically in figure 2. It is assumed that the splashback occurs over angular range θ centered about the surface normal. For a perpendicular impact ($\beta = 90°$), it is assumed that 50% of the mass of the incident drop is splashed back over an angular range of $\theta = 120°$ as droplets of diameter 10 μm and with an initial velocity equal to that of the incident drop. As a tangential impact is approached ($\beta = 0°$), the angular range of splashback, the fraction of mass splashed back and the initial velocity of the splashed back droplets all go to zero. Between the two extremes of a perpendicular and tangential impact, a linear variation of splashback parameters is assumed according to the angle of incidence.

The splashback model is a very critical part of the numerical scheme, since it affects the momentum loss that the boundary experiences in accelerating the splashed back droplets. However, the splashes are complex processes. The characteristics of the splashed back droplets vary with the incidence angle and velocity of the incident drop and even change during the splash process. Insufficient data exist to completely and accurately characterize the splash. Our primary interest is to determine how a plausible distribution of splashed back droplets can alter the boundary layer and change the lift, drag and stall characteristics of the airfoil.

2.3. *Interphase Coupling*

Momentum coupling between the fluid and particulate phases is due to interphase drag forces. This is explicitly accounted for in the Lagrangian equations of motion for particle trajectories, however, a momentum source/sink "body force" term must be added to the Navier–Stokes equations to account for the particle effect on the fluid phase. The momentum source–sink term is determined by tabulating the particle drag throughout the flow field.

Cells are defined centered around each gridpoint and dimensionless particle drag distributions are tabulated on a per volume basis for each cell as

$$\mathbf{D} = \frac{1}{V_{\text{cell}}} \sum_{i,j} \left[\frac{1}{2} \pi \frac{r_{\text{p}}^2}{c^2} C_{\text{D}} |\mathbf{V} - \mathbf{V}_{\text{p}}| (\mathbf{V} - \mathbf{V}_{\text{p}}) \right] \dot{N}_{ij} \Delta t_{\text{p},ij}. \qquad [18]$$

Velocities in [18] are averaged over the time step, V_{cell} is the dimensionless volume of the cell (scaled by the cube of the airfoil chord length), the particle drag coefficient C_{D} is determined by [4] and averaged over the time step, $\dot{N}_{ij}$ is the raindrop number flow rate from [14] associated with the particle and $\Delta t_{\text{p},ij}$ is the residence time of the particle in the cell. The bracketed term in [18] represents the dimensionless drag force acting on a tracked particle. The sum is over all particles that transverse the cell for all diameter intervals i and all particle entry locations j. The quantity calculated in [18] is subtracted from the right hand side of the Navier–Stokes equations in the air flow code FMC1.

3. RESULTS AND DISCUSSION

The steady state fluid and particle fields are determined by alternately solving for each field, each time using the most recently calculated interphase coupling terms. Initially, the clean air flow field

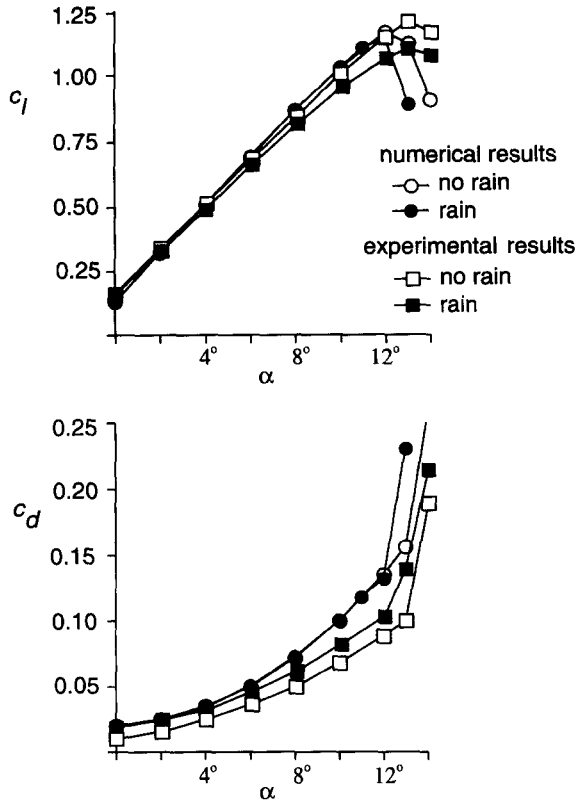

Figure 3. Numerically determined lift (c_l) and drag (c_d) coefficients vs angle of attack (α) for a rainfall rate corresponding to LWC = 25 g/m^3 compared to the experimental results of Bezos *et al.* (1992).

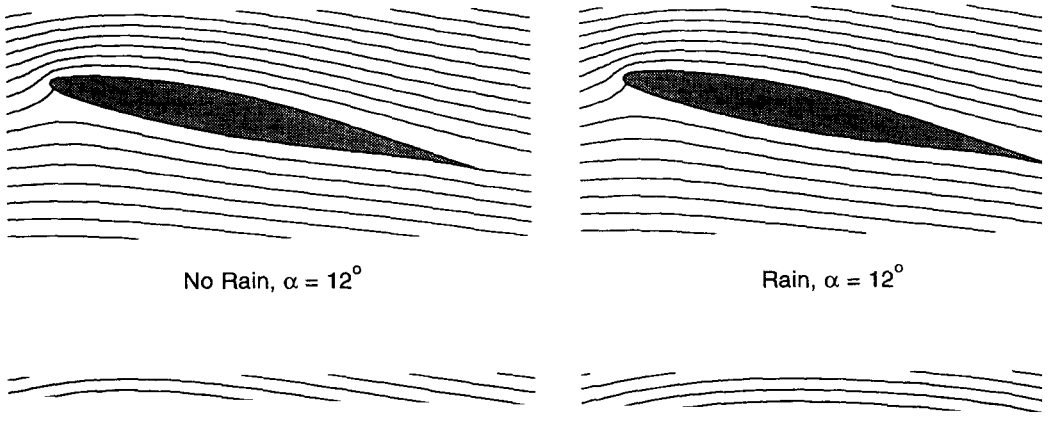

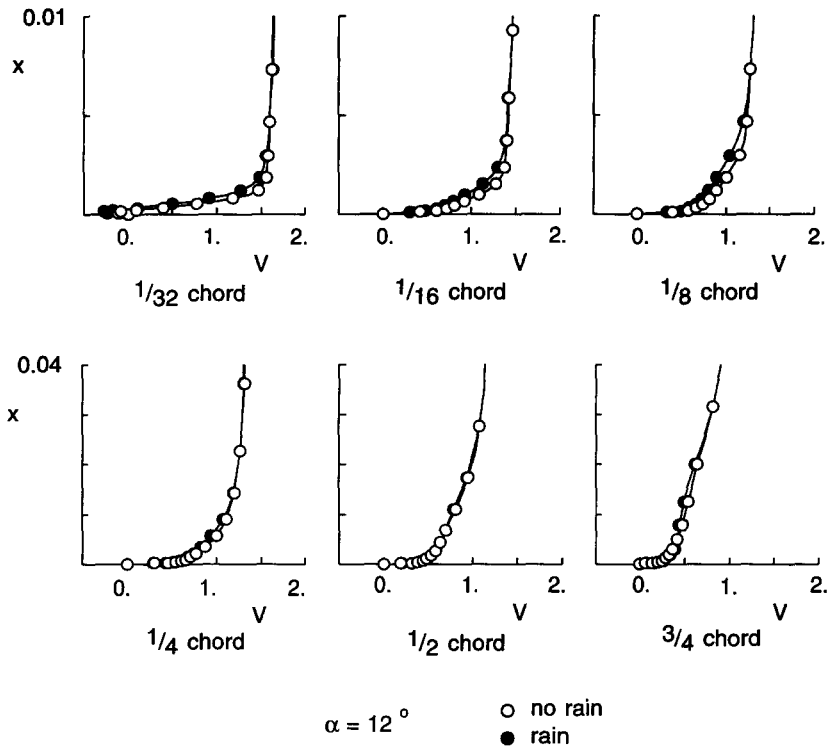

Figure 5. Boundary layer velocity profiles at six chordwise positions on the upper surface of the airfoil. Position is measured from the leading edge. Dimensionless velocity is plotted vs dimensionless distance from the airfoil surface.

(no rain) is determined, then particles are tracked through this field and the interphase coupling terms from [18] are tabulated throughout the grid. The air flow field is then redetermined, this time accounting for interphase coupling, and particle trajectories and interphase coupling terms are recalculated using the modified air flow field. This process is repeated until a stationary solution is reached, i.e. until the airfoil lift coefficient does not change between iterations. At low angles of attack, five or fewer iterations were required to achieve convergence. However, at angles of 11° or greater, up to thirty iterations were needed. At higher angles of attack, an underrelaxation factor was required for stability; thus at each step, the air flow field was updated by only a fraction of the calculated amount. Initially, an underrelaxation factor of 0.05–0.1 was used, but convergence was improved if this was gradually increased to 1 as the simulation progressed.

Rain-induced changes in airfoil performance coefficients are shown in figure 3 and compared to the experimental results of Bezos *et al.* (1992) for the same airfoil at the same Reynolds number but a smaller chord length airfoil (0.762 m). A rainfall rate corresponding to a LWC of 25 g/m^3 was used in both simulations. In each case, the raindrop size distributions were concentrated toward smaller diameter drops, but the drops in the experimental study were of overall smaller diameter than those in the numerical simulation. The smaller diameter drops and airfoil chord length in the experimental study are not expected to have a large effect on the results presented here, and in any case, the scaling of drop diameters with respect to chord length will tend to be preserved.

The experimental results in figure 3 show a decrease in lift and an increase in drag at most angles of attack with the lift penalty reaching a maximum at stall. The numerical results, however, show a rain induced more severe stall but no change in airfoil performance until stall is reached. A rain induced decrease in stall angle of attack has been observed experimentally for this airfoil at a higher Reynolds number of 3.4×10^6 and a LWC of 30 g/m^3 (Bezos *et al.* 1992).

Streamline patterns are shown in figure 4. At an angle of attack of 12°, rain has induced no obvious change in the flow, however, when the angle of attack is increased to 13°, rain causes massive separation on the upper surface of the airfoil.

Boundary layer velocity profiles at six chordwise positions on the upper surface are shown in figure 5. Near the leading edge, the deceleration of the boundary layer by splashed back droplets relative to the boundary in the absence of rain is clearly seen. Moving downstream, the boundary layer appears to recover, but at the 3/4 chord position, separation appears to be imminent.

Droplet distributions around the airfoil are shown in figure 6. At an angle of attack of 4°, splashed back droplets are carried over both the upper and lower surfaces of the airfoil, staying

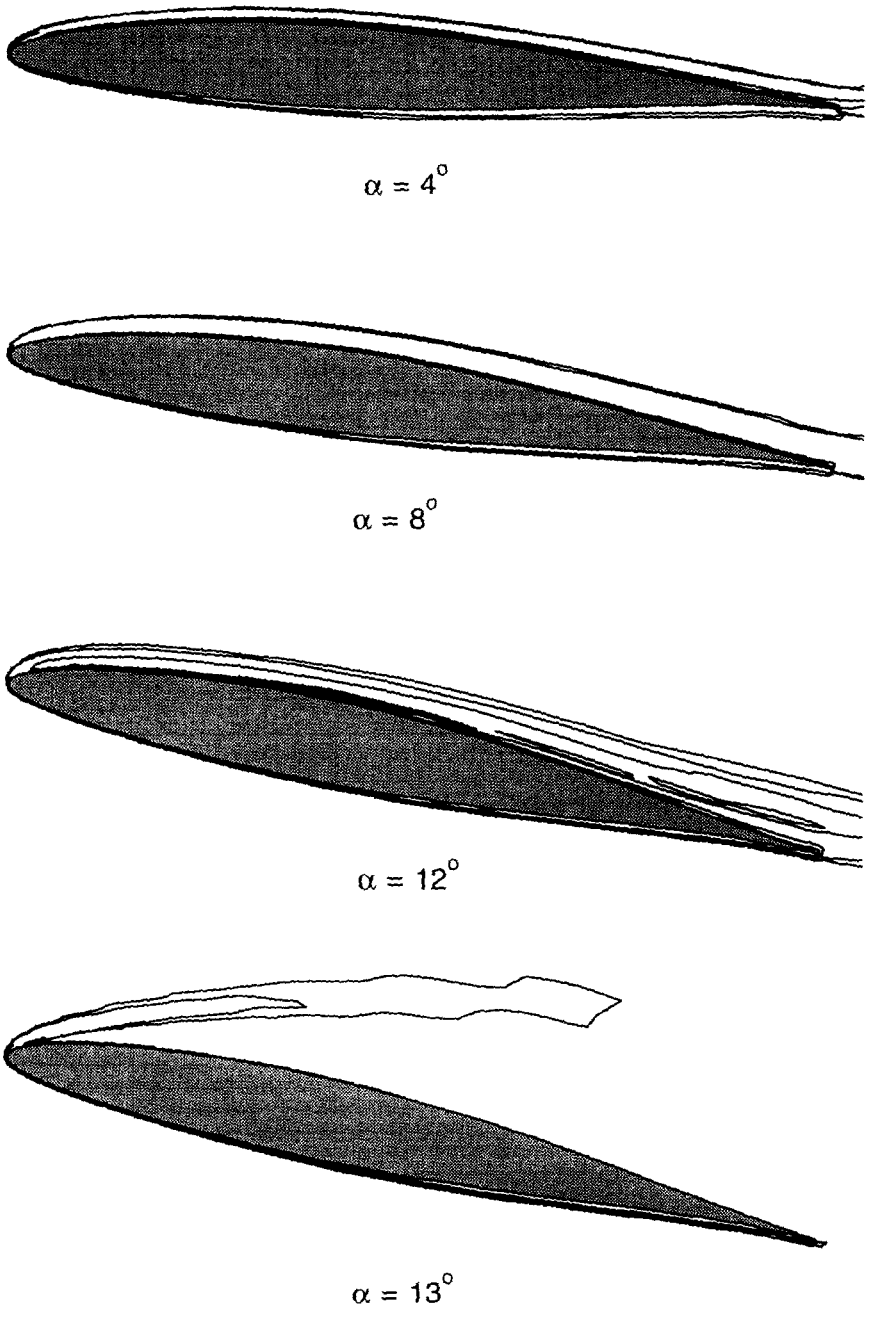

Figure 6. The distribution of splashed back droplets around the airfoil.

fairly close to the upper surface. As the angle of attack is increased, the droplets tend to occupy a wider area on the upper surface. At the highest angle of attack of 13°, droplets are carried over the separated region. Figure 6 shows the presence of a droplet "ejecta fog" layer at the leading edge of the airfoil and a "water bow wave" extending over the airfoil surface, both of which have been reported in experimental investigations (Bezos *et al.* 1992). The patterns shown in this figure should be viewed qualitatively, however, since the grid is non-uniform and resolution decreases away from the airfoil surface. Turbulent dispersion of the small splashed back droplets is not modeled, thus the contours show mean trajectories.

Several splashback models other than the one presented here have been used in numerical simulations. It was found that the severity of the splashback can be increased primarily by decreasing the size of the splashed back droplets (thus more droplets are splashed back) and by increasing the fraction of the incident mass splashed back. For less severe splashbacks, there may be no observable change in airfoil performance, however, when a performance loss was observed, it was similar to the results presented here. No splashback models resulted in any change in airfoil performance prior to the point of stall, however, a 1–2° rain-induced more severe stall was observed in many cases.

In conclusion, two physical phenomena have been hypothesized to be responsible for the degradation of airfoil performance in rain, the loss of boundary layer momentum to splashed back droplets and the effective roughening of the airfoil surface due to an uneven water film. Only the first of these is modeled here, and the numerical results show only part of the airfoil performance loss in rain that has been observed experimentally, a rain-induced more severe stall. Any decrease in lift prior to stall is not captured by this simulation, and thus may be due to the uneven water film on the airfoil surface. The distribution of splashed back droplets around the airfoil as predicted by the numerical scheme is similar to that observed experimentally.

Acknowledgement—This project was supported by the Heavy Rain Research Group in the Subsonic Aerodynamics Branch, Applied Aerodynamics Division, NASA/Langley Research Center (NASA contact #NAG-1-1232).

REFERENCES

Anderson, D. A., Tannehill, J. C. & Pletcher, R. H. 1984 *Computational Fluid Mechanics and Heat Transfer*, pp. 252–253. Hemisphere, New York.

Bezos, G. M. & Campbell, B. A. 1993 Development of a large-scale, outdoor, ground-based test capability for evaluating the effect of rain on airfoil lift. NASA TM-4420.

Bezos, G. M., Dunham, R. E., Gentry, G. L. & Melson, W. E. Jr 1992 Wind tunnel aerodynamic characteristics of a transport-type airfoil in a simulated heavy rain environment. NASA TP-3184.

Bezos, G. M., Dunham, R. E., Gentry, G. L. Jr & Melson, W. E. Jr 1987 Wind tunnel results of heavy rain on airfoil performance. AIAA-87-260.

Bilanin, A. J. 1987 Scaling laws for testing airfoils under heavy rainfall. *J. Aircraft* **24,** 31–37.

Crowe, C. T., Sharma, M. D. & Stock, D. E. 1977 The particle-source-in-cell (PSI-Cell) model for gas–droplet flows. *J. Fluids Engng* **99,** 325–332.

Decker, R. & Shafer, C. F. (Eds) 1989 Mixing and demixing processes in multiphase flows with application to propulsion systems. NASA CP-3006.

Dukowicz, J. K. 1980 A particle–fluid numerical model for liquid sprays. *J. comp. Phys.* **35,** 229–253.

Dunham, R. E. Jr 1987 The potential influence of rain on airfoil performance. Lecture presented at the Von Karman Institute for Fluid Dynamics, lecture series entitled *Influence of Environmental Factors on Aircraft Wing Performance.*

Durst, F., Milojevic, D. & Schönung, B. 1984 Eulerian and Lagrangian predictions of particulate two-phase flows: a numerical study. *Appl. Math. Model.* **8,** 101–115.

Feo, A. 1987 Rotating arms applied to studies of single angular drop impacts. AIAA-87-0257.

Hansman, R. J. Jr & Craig, A. P. 1987 Low Reynolds number tests of NACA 64-210, NACA 0012, and Wortmann FX67-K170 airfoils in rain. *J. Aircraft* **24,** 559–556.

Hartwich, P-M. & Hall, R. M. 1990 Navier–Stokes solutions for vortical flows over a tangent-ogive cylinder. *AIAA J* **28,** 1171–1179.

Hartwich, P.-M. & Hsu, C.-H. 1988 High resolution upwind schemes for the three-dimensional Navier–Stokes equations. *AIAA J.* **26,** 1321–1328.

Joss, J. & Waldvogel, A. 1969 Raindrop size distribution and sampling size errors. *J. Atmos. Sci.* 26, 556–569.

Wallis, G. B. 1969 *One-dimensional Two-phase Flow*. McGraw–Hill, New York.